Kobe University Repository : Kernel

PDF issue: 2025-12-04

Charge Carrier Dynamics in Sr-Doped NaTaO3 Photocatalysts Revealed by Deep Ultraviolet Single-Particle Microspectroscopy

Mizutani, Seigo ; Karimata, Izuru ; An, Longjie ; Sato, Takamasa ; Kobori, Yasuhiro ; Onishi, Hiroshi ; Tachikawa, Takashi

(Citation)
Journal of Physical Chemistry C,123(20):12592-12598

(Issue Date)
2019-05-23

(Resource Type)
journal article

(Version)
Accepted Manuscript

(Rights)
This document is the Accepted Manuscript version of a Published Work that appeared in final form in Journal of Physical Chemistry C, copyright © American Chemical Society after peer review and technical editing by the publisher. To access the final edited and published work see https://doi.org/10.1021/acs.jpcc.9b01929

(URL)
https://hdl.handle.net/20.500.14094/90006088

Charge Carrier Dynamics in Sr-Doped $NaTaO_3$ Photocatalysts Revealed by Deep UV Single-Particle Microspectroscopy

Seigo Mizutani,[†] Izuru Karimata,[†] Longjie An,[†] Takamasa Sato,[†] Yasuhiro Kobori,[†,‡] Hiroshi Onishi,[†,] and Takashi Tachikawa[†,‡,*]*

[†] Department of Chemistry, Graduate School of Science, Kobe University, 1-1 Rokkodai-cho, Nada-ku, Kobe 657-8501, Japan

[‡] Molecular Photoscience Research Center, Kobe University, 1-1 Rokkodai-cho, Nada-ku, Kobe 657-8501, Japan

[*]E-mail: tachikawa@port.kobe-u.ac.jp (T.T.); oni@kobe-u.ac.jp (H.O.)

TEL: +81-78-803-5736 (T.T.); +81-78-803-5657 (H.O.)

Abstract. Among various metal oxides, sodium tantalate ($NaTaO_3$) is one of the best semiconductors for achieving efficient photocatalytic water splitting. However, the primary mechanism responsible for increasing the reaction rate up to an order of magnitude by specific metal doping and surface modification with co-catalysts has not been elucidated yet. In order to clarify the underlying mechanism, we explored the structure-dependent photoluminescence (PL) of pristine and Sr-doped $NaTaO_3$ crystals at the (near) single-particle level using a time-resolved deep ultraviolet fluorescence microscope. Combined with transmission electron microscope (TEM) techniques, the PL characteristics of individual particles were directly linked to the dopant concentrations in each particle, allowing us to unravel the complex effects of Sr-doping on the charge carrier dynamics. Furthermore, we investigated the photocatalytic reduction reaction for a single Sr-doped $NaTaO_3$ particle to gain critical information related to dopant-driven electron migration, which is a key process for efficient photocatalysis.

Introduction

Heterogeneous photocatalysts have been studied for a long time as a countermeasure to environmental and energy problems, in which sunlight is utilized to promote solar fuel reactions such as hydrogen production and the reduction of carbon dioxide.[1-4] Hitherto, no photocatalyst system has reached a level that can be put to practical use. The discovery of an optimized structure with a high photocatalytic activity has thus been a challenging issue for many researchers. In 2000, Kudo and Kato reported that the photocatalytic activity of $NaTaO_3$ is drastically increased by doping with La^{3+} and modification with a NiO co-catalyst, yielding the highest quantum yield (ca. 50% at 270 nm) for water splitting under ultraviolet light (UV)

irradiation without the use of sacrificial reagents.[5] This enhancement was found to be related to the suppressed recombination of photogenerated charge carriers by specific surface nanostructures with characteristic steps created during the doping process.[6] Since then $NaTaO_3$ photocatalysts doped with alkaline-earth metal cations (Ca, Sr, and Ba) have been developed.[7-8] In addition to $NaTaO_3$, water splitting efficiency of $SrTiO_3$ was enhanced up to 69% by doping with Al^{3+}.[9] The perovskite-type metal oxides would be potentially good host materials for doping with metal cations to achieve water splitting efficiency close to unity. However, mechanisms behind the increased efficiency are still unknown.[10] Because $NaTaO_3$ crystals have a large band gap (approximately 4.0 eV) that responds only to UV light with a wavelength region lower than 310 nm,[11] their application as the photocatalyst for solar fuel systems is impractical. However, if the physicochemical mechanism underlying their extremely high efficiency can be clarified and applied to other photocatalysts with visible-light response, it will be a significant breakthrough towards realizing their practical applications.[12]

The photophysical processes in photocatalysis leading to water splitting are divided as follows: (1) generation of an electron–hole pair by photon absorption; (2) separation into free charge carriers, followed by charge transport through the bulk; (3) charge carrier extraction at the surface; and (4) catalytic reactions associated with mass transfer of reactants and products.[13-14] Among these processes, significant electron–hole recombination leading to the short lifetime and diffusion length of carriers in a catalyst remains a major barrier to achieving a high conversion efficiency of light to chemical energy. In other words, the performance of photocatalysts is dependent on the delivery of the photogenerated charges to the catalytic sites without significant loss, while keeping their potential energies for subsequent reactions, i.e., oxidation and reduction of H_2O. In this respect, it is plausible that the metal doping in $NaTaO_3$ changes not only the

crystal structures, including the defects, but also the electric structures, providing the driving force for charge migration.

The main subject of this study is to elucidate the impacts of metal doping on the charge carrier dynamics in perovskite-type metal oxides. Sr-doped $NaTaO_3$ was selected as a model photocatalyst because of its relatively well-characterized structures.[15-17] For this purpose, we have constructed a deep UV fluorescence microscope (DUV-FM) with a 266 nm laser as an excitation source for single $NaTaO_3$ particles. Photoluminescence (PL) microspectroscopy is a powerful method for defining the nature and dynamics of excitons or charge carriers through the observation of emission spectra and lifetimes at high temporal and spatial resolutions.[18-21] The PL properties are closely associated with the band structures of semiconductors, the types of internal/surface defects, and the chemisorbed species.[22] Furthermore, in-site observation of emission from single particles or single molecules can provide useful information on the structural heterogeneity, fluctuation in reactivity among the catalyst particles, and the intrinsic correlation between variables.[23-25] The relationship between the PL and the structural characteristics of the same Sr-doped $NaTaO_3$ particles was directly examined by combining the DUV-FM with transmission electron microscope (TEM) techniques. Furthermore, in-site observation of the photocatalytic reduction reaction of a fluorogenic probe over a single Sr-doped $NaTaO_3$ particle was performed to reveal the involvement of long-range electron migration driven by spatially and energetically-controlled doping, uncovering the mystery of metal-doped $NaTaO_3$.

Results and Discussion

The pristine and Sr-doped $NaTaO_3$ samples were synthesized by solid-state methods, (hereinafter referred to as NTO-SS and Sr-NTO-SS, respectively (Figure 1a).[15] As visualized in scanning electron microscope (SEM) images of Figure 1b, NTO-SS particles are spherical cubes with sizes of 2–6 μm in diameter. After doping with Sr at 5 mol%, the particle size was reduced to 0.5–1 μm due to the lattice mismatch in a particle comprising a Sr-rich solid-solution shell over a Sr-poor core.[15]

To achieve (near) single-particle observations, an isolated single particle or a small aggregate with a size of below a few micrometers was selected from optical transmission and emission images acquired with a spatial resolution of ~270 nm per pixel (Figure 1c). In addition, only $NaTaO_3$ PL over an area of ~2 μm^2 was passed through a pinhole and detected by a CCD camera with a spectrograph or a single-photon avalanche diode for spectral or lifetime measurements, respectively (Figure S1). The experiments were performed in ambient air, since no significant effects of moisture and gaseous oxygen on the PL characteristics were observed. The low reactivity toward oxygen is probably due to slower electron transfer on the microsecond time scale.[26]

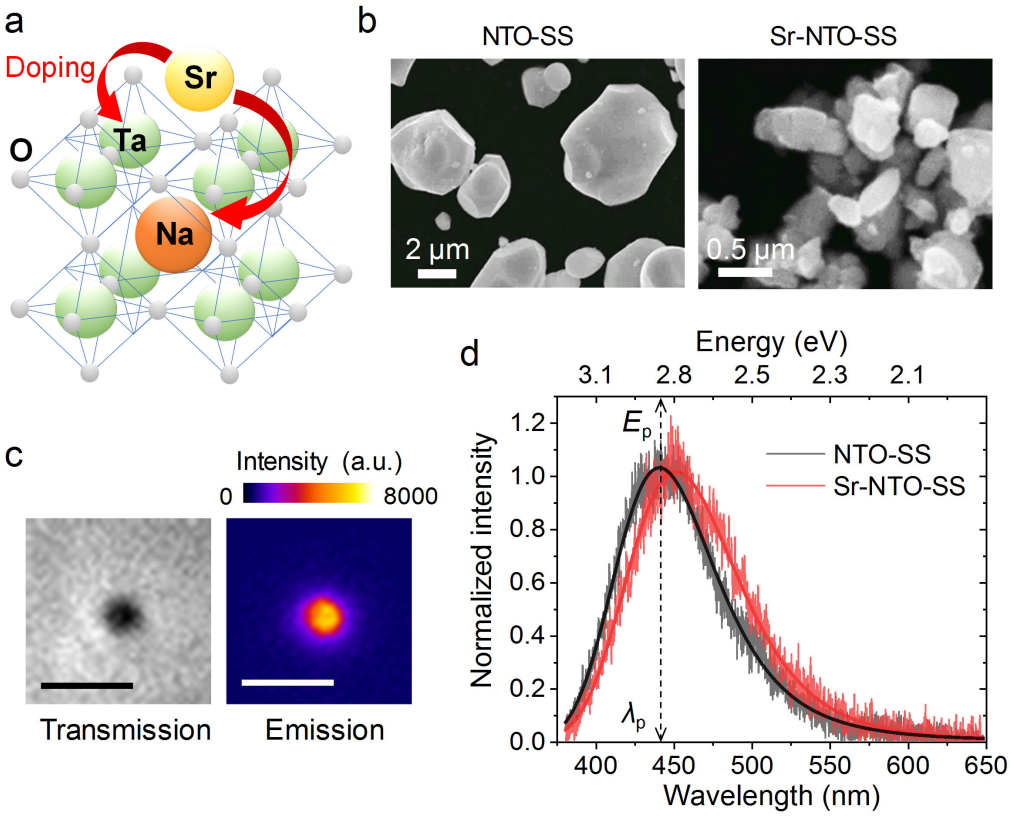

Figure 1. (a) Perovskite structure of $NaTaO_3$. The Sr cations are doped into the Ta and Na sites via solid-state synthesis.[15] (b) SEM images of NTO-SS and Sr-NTO-SS particles. Scale bars are 2 μm. (c) Optical transmission and PL images of a single NTO-SS particle. Scale bars are 5 μm. (d) Normalized PL spectra of NTO-SS and Sr-NTO-SS particles. Bold lines represent the results by modified Gaussian fitting based on eq 1. The ω values are 0.17 eV and 0.19 eV, and the μ values are 0.15 eV and 0.14 eV for NTO-SS and Sr-NTO-SS, respectively. See eq 1 and main text for details. The broken line indicates the peak wavelength (λ_p) and energy (E_p) for NTO-SS.

Figure 1d shows the normalized PL spectra of typical particles under 266 nm laser irradiation. Both samples have a broad structureless luminescence band centered at 440–450 nm with a large Stokes shift, while Sr-NTO-SS exhibits a much weaker PL intensity by a tenth as compared with those of NTO-SS (Table 1). According to the literature,[27-29] the observed PL band is ascribed to a self-trapped exciton (STE) (or a small polaron in its own lattice distortion field),[30] such as the

Ta^{4+}-O^{-} state in TaO_6 octahedral, or bound-exciton states at impurities or defects. The observed spectra match well with an exponentially modified Gaussian distribution, which is defined by the following convolution integral:[31-33]

$$I(E) = \frac{A}{\mu}\exp\left[\frac{1}{2}\left(\frac{\omega}{\mu}\right)^2 - \frac{E-E_c}{\mu}\right]\int_{-\infty}^{Z}\frac{1}{\sqrt{2\pi}}e^{-x^2/2}dx \quad (1)$$

where A is the amplitude of the emission, ω is the peak width of the Gaussian component, μ is the modification or skewness factor, which determines the amplitude of the asymmetry in the line shape, E and E_c are the photon and center energies, respectively, and x is the dummy variable of integration. Z is given by

$$Z = \frac{E-E_c}{\omega} - \frac{\omega}{\mu} \quad (2)$$

The ω and μ values, which provide information regarding the population of the carriers, are determined as given in the caption of Figure 1. No significant difference was observed between two samples, suggesting that a similar number of phonon levels were involved in the transition.

STE luminescence has been reported for many metal oxides such as TiO_2 and $SrTiO_3$, and its intensity is known to be highly suppressed by the increase in temperature due to the electron-hole dissociation.[34-35] For orthorhombic $NaTaO_3$, however, the thermal activation energy of the STE band was reported to be 86 meV,[28] which is higher than the thermal energy at room temperature (26 meV). This suggests that 94% of excitons cannot be dissociated to become free carriers (i.e., electrons and holes) according to the Boltzmann distribution under the present conditions and would thus hinder the photocatalytic activity.

It should be noted here that the peak position is strongly dependent on the synthesis methods. The samples prepared by the hydrothermal method (HTM) exhibit a peak at approximately 550 nm (Figure S2). $KTaO_3$ shows the similar PL band at approximately 590 nm, which was proposed to originate from the O vacancies.[36] These results imply that several types of defects

are involved in the photophysical processes of $NaTaO_3$ synthesized by HTM; this probably lowers the efficiency of the photocatalytic reactions via trap-mediated recombination.[15, 37]

Although the PL peak wavelength allows us to inspect the electronic state of charge carriers, the difference (~0.03 eV on average) between non- and Sr-doped $NaTaO_3$ samples is too small to be statistically analyzed by ensemble experiments because of structural heterogeneities among the particles (Table 1). We thus attempted to clarify the relationship between the PL characteristics and Sr concentration in individual doped $NaTaO_3$ particles by utilizing the combined DUV-FM and TEM, which was capable of conducting quantitative elemental analysis with an energy dispersive X-ray spectrometer (EDS). For this purpose, Sr-NTO-SS particles were spin-coated on a TEM grid with windows covered by 40-nm silicon oxide film (Figure S3). To avoid any structural modification of the sample by the electron beam, the PL measurements were first performed, followed by the TEM-EDS analysis. The relative concentration of Sr contained in each particle was estimated from the peak intensities of the Na-Kα, Ta-Lα, and Sr-Kα lines in the EDS spectrum, and the exact Sr concentration was then determined using a calibration curve generated from the data of the mixtures of Ta_2O_5 and $SrTiO_3$ with known ratios (Figure S4,5).

Table 1. Structural and PL Characteristics of the Samples [a]

sample	d, μm	$\overline{I_p}$, a.u. [b]	$\overline{\lambda_p}$, nm ($\overline{E_p}$, eV) [b]	$\overline{\tau}$, ns
NTO-SS	2–6	1810 ± 700	453 ± 9 (2.74 ± 0.05)	9.9 ± 2.2
Sr-NTO-SS	0.5–1	188 ± 109	447 ± 9 (2.77 ± 0.06)	3.8 ± 1.1

[a] The errors represent the standard deviation of the data.

[b] The mean values of peak wavelengths and energies.

The dark-field TEM images shown in Figure 2a were obtained for two different Sr-NTO-SS particles in the same window, together with their PL and EDS spectra (Figure 2b). Particle A has a single crystal-like structure with a nearly flat surface, while particle B has an irregular shape and a step-terrace structure on the surface. Notably, there is a substantial (approximately three times) difference in the PL intensity between them even though their size is almost the same. In the EDS spectra, there is a clear difference in the intensity of the Sr signal in which particle B exhibits a much higher intensity than that of particle A. According to the previous study,[16] Sr-doped $NaTaO_3$ particles have no obvious step-terrace structure on the surface when the dopant concentrations are less than 1.0 mol%. The step-terrace structure on particle B seems to originate from the formation of an Sr shell by doping an excess amount of Sr.[15-16] The Sr concentrations of particles A and B are estimated to be 0.4 mol% and 1.5 mol%, respectively, suggesting that the formation of the Sr shell lowers the PL intensity and thus suppresses the radiative recombination. The direct comparison of PL and the structural characteristics between NTO-SS and Sr-NTO-SS not only supports our speculation based on the averaged data, but also reveals an interesting tendency that is masked by the sample heterogeneities, as demonstrated below.

Figure 2d plots the peak energies of the PL spectra against the Sr concentrations for each particle. Although the Sr concentration for each particle varies, the average concentration is close to the statistical value of approximately 5 mol%, determined by X-ray fluorescence spectroscopy. When the doping amount of Sr increases, the peak energy tends to increase from 2.75 to 2.85 eV and then decrease in the range of 3–9 mol%. This concentration dependence is similar to the one that electron population in Sr-NTO-SS increased with increasing Sr concentration and then decreased at Sr concentrations above 1.8 mol%.[15, 38] It should be noted that the blue shift of approximately 0.1 eV in the lower concentration region is comparable to the increase of the band

gap energy (~0.1 eV) by Sr-doping.[15, 38] Meanwhile, the higher doping amount (> 3 mol%) results in the red shift of the PL peak, possibly due to delocalization of the excited states and/or involvement of deeper trap states caused by crystal deformations and surface reconstructions.[28, 39] It was suggested that excess K-doping (> 5 mol%) creates defect states in K-doped $NaTaO_3$, thus lowering the photocatalytic activity.[40]

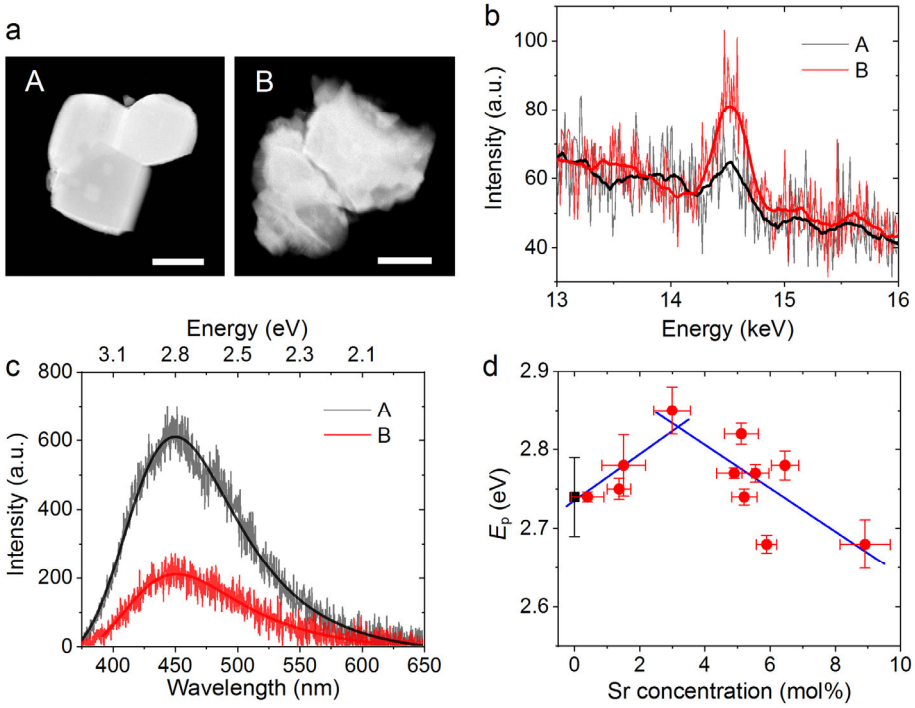

Figure 2. (a) Dark-field TEM images of different Sr-NTO-SS particles synthesized in the same batch. Scale bars are 200 nm. (b) EDX spectra of particles A and B in panel a. The bold lines indicate the spectra after smoothing. (c) PL spectra of particles A and B in panel a. Bold lines represent the results by modified Gaussian fitting based on eq 1. (d) Relationship between the Sr concentrations and PL peak energies observed for individual Sr-NTO-SS particles (red circles). The average PL peak energy obtained for NTO-SS is also shown as a black square. The blue lines are linear fits to the data in the Sr concentration ranges of 0–3 mol% and >3 mol%.

To investigate the impact of Sr-doping on the charge carrier dynamics in $NaTaO_3$, the PL lifetime measurements were performed with a 266-nm pulsed laser (pulse width; 1.0-ns FWHM). Figure 3a shows examples of decay profiles obtained for single NTO-SS and Sr-NTO-SS particles. Each decay curve was fitted by a multi-exponential function with three components. The results are summarized in Table S1 along with the intensity-weighted average lifetimes ($\langle\tau\rangle$) calculated from the equation: $\langle\tau\rangle = (a_1\tau_1^2 + a_2\tau_2^2 + a_3\tau_3^2)/(a_1\tau_1 + a_2\tau_2 + a_3\tau_3)$, where τ_i and a_i are the lifetime and amplitude of each component (i = 1, 2, or 3), respectively. The $\langle\tau\rangle$ values of 11 ns and 4.2 ns were determined for NTO-SS and Sr-NTO-SS in Figure 3a, respectively. As shown in Figure 3b, the different particles exhibit widely varying lifetimes, which will be discussed later. The mean values ($\overline{\tau}$) of the $\langle\tau\rangle$ values obtained for individual particles show an obvious difference between these two samples (Table 1). According to the fact that the mean PL peak intensity ($\overline{I_{\mathrm{p}}}$) decreased by Sr-doping, the shortened lifetime of Sr-NTO-SS suggests an additional non-radiative decay pathway. The rate of PL quenching (k_{q}) by the dopant-induced dissociation of the STEs can thus be calculated as 1.5×10^8 s^{-1} from the equation $k_{\mathrm{q}} = \overline{\tau}_{\mathrm{Sr-NTO-SS}}^{-1} - \overline{\tau}_{\mathrm{NTO-SS}}^{-1}$ (Table 1).

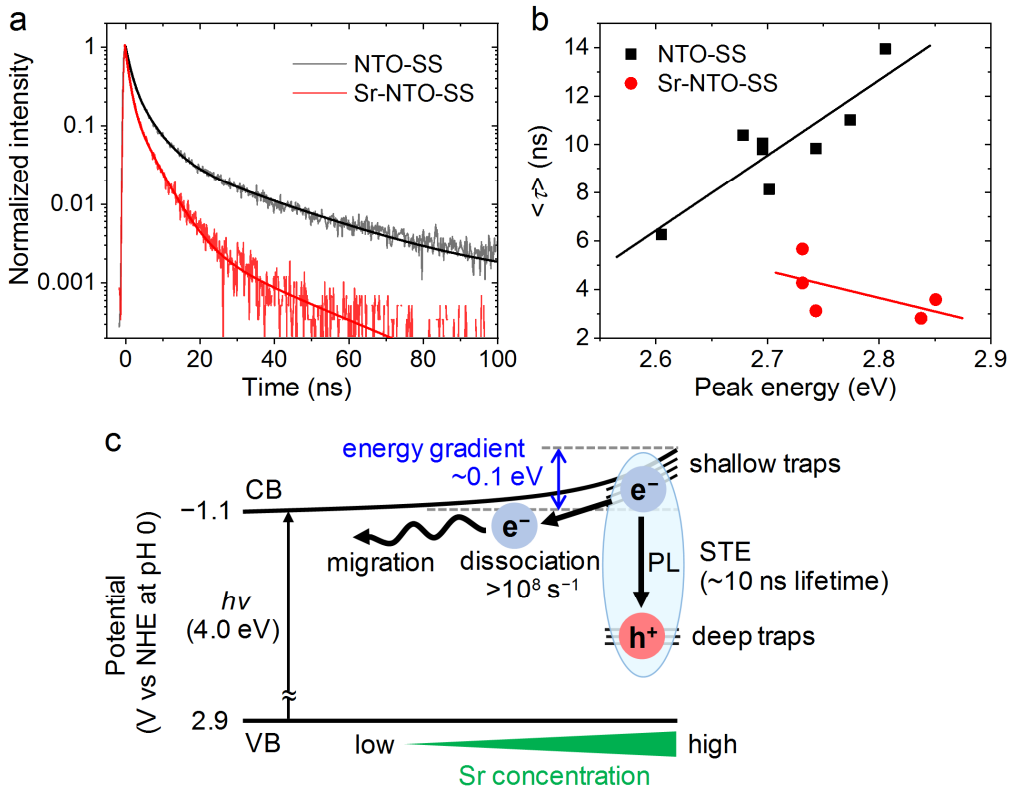

Figure 3. (a) Normalized PL decay profiles of NTO-SS (black) and Sr-NTO-SS (red) particles. Solid lines indicate triple exponential decay fit to the data. (b) The relationship between the PL peak energy and lifetimes obtained for individual NTO-SS (black squares) and Sr-NTO-SS (red circles) particles. Solid lines represent linear fitting of the data. (c) Proposed mechanism of the charge recombination and separation in Sr-doped $NaTaO_3$.

The pristine $NaTaO_3$ crystals synthesized by solid-state method have an orthorhombic *Pcmn* phase, which is a direct semiconductor.[15, 29] It was reported, however, that the direct band gap is changed into an indirect band gap when $NaTaO_3$ is doped with La.[41-42] The recombination of electron–hole pairs is usually much slower in the systems with an indirect band gap. The results in Figure 3b obviously oppose this tendency.

Furthermore, the Ta–O–Ta bond angle (~157° for orthorhombic $NaTaO_3$[43]) affects the delocalization of the photogenerated electrons and thus the photocatalytic activity, i.e. the closer the bond angle is to the ideal 180°, the higher is the mobility of the charge carriers in tantalates and hence the higher is the activity.[11, 39] For instance, Hu et al. attributed the lower PL intensity of a monoclinic $NaTaO_3$ than an orthorhombic one to the enhanced charge separation due to the increase of the Ta–O–Ta bond angle.[29] It was further suggested that the photocatalytic activity of $NaTaO_3$ is improved by replacing some Na ions with larger K ions to produce $Na_{1-x}K_xTaO_3$ photocatalysts (x = 0.05) with a pseudo-cubic phase in which the 180° bond angle of Ta–O–Ta in the pseudo-cubic phase facilitates the separation of photogenerated charges for effective water splitting.[40] Further K-doping (with $x > 0.05$) leads to impurity formation, which bends the Ta–O–Ta linkage and creates defect states, thus lowering the photocatalytic activity of $Na_{1-x}K_xTaO_3$.[40]

A larger amount of delocalization implies that the electron–hole pairs easily separate and migrate to active sites for photocatalysis, while a few electron–hole pairs have recombined. As already shown in Figure 3b, the lifetime of NTO-SS became shorter at lower emission photon energies. This is probably due to separations of the electrons and holes from the STEs at more delocalized states resulting in the free carriers and/or trapping of the charge carriers at the intrinsic surface states. On the other hand, Sr-NTO-SS particles possessing peaks at higher energies (i.e., shorter wavelengths) have much shorter lifetimes compared with ones with peaks at lower energies (i.e., longer wavelengths). This result cannot be explained by the aforementioned mechanism related to the increased Ta–O–Ta bond angle leading to delocalization.

Recently, Onishi and co-workers proposed an alternative mechanism for the enhanced photocatalytic activity of Sr-doped $NaTaO_3$.[15, 38] The conduction band (CB) of pristine $NaTaO_3$

mainly comprises Ta 5d orbitals.[44-45] By replacing the Ta sites with Sr cations, SrO_6 octahedra are formed in the corner-shared network of the TaO_6 octahedra.[17] The embedded SrO_6 octahedra hinder the overlap of the Ta 5d orbitals, which shifts the CB minimum to higher energy by ~0.1 eV,[15] as is also evident from the result in Figure 2d. The concentration gradient of the Sr cations doped at the Ta sites induces the energy gradient of the CB minimum. Hence, the photogenerated electrons in the CB or at shallow sites, which are dissociated from the STEs, diffuse from the surface to the bulk along the energy gradient, leaving the holes. In Figure 3b, the decrease in the PL lifetime for the higher PL peak energy implies the accelerated STE dissociation by the increase in this energy gradient. This hypothesis is a promising mechanism for the enhancement of the quantum efficiency induced by metal-doping[38] and is compatible with our findings (Figure 3c).

In order to confirm the reactivity of photogenerated charges, PL quenching tests were performed. As shown in Figure S6, no significant change in the PL intensity was observed for Sr-NTO-SS particles by dropping methanol as a hole scavenger onto the cover glass,[6] whereas the intensity was considerably reduced by the addition of IO_3^- as an electron scavenger;[46] this result is in accordance with the above proposed electron-transfer mechanism using the energy gradient in Figure 3c. Considering that most surface-trapped holes in TiO_2 are captured by adsorbed alcohols within several hundred picoseconds,[47] the photogenerated holes in Sr-NTO-SS may have poor mobility due to the higher effective masses[41] or trapping in bulk. A similar interpretation was adopted to explain the fact that the STE luminescence from TiO_2 at approximately 420–440 nm does not respond to exposures to ethanol solvent.[48] According to the density functional theory (DFT) calculations,[44] O vacancy states close to the CB minimum are presumed to be the primary shallow traps for mobile electrons. For the trap site of the hole, there

are defects with different formation energies.[44] Among them, Na antisite (Na_{Ta}) and Ta vacancy (V_{Ta}) have the lowest formation energies and their states are close to the valence-band (VB) maximum. The deep hole-trap characteristic is consistent with the E_p energy, which is much smaller than the bandgap, assuming that the electron in the STE resides at the energy level closed to the CB. Longo et al. reported that the symmetry break induces the localized electronic levels in the VB, leading to the visible emission in perovskite-type compounds.[49] The presence of deep hole traps is not clear yet for $NaTaO_3$, but these states should be involved in the photophysical processes in photocatalysis.

Here, a question arises: can the escaped electrons move to the surface again and react with the substrates (e.g., H^+ during water splitting)? To answer this question, we directly observed the photocatalytic reduction reaction on a single particle using a fluorogenic probe MS-DN-BODIPY (Figure 4a).[50] Prior to the single-particle observation, the bulk experiments were performed (Figure S7). As depicted in Figure 4b, a much higher reactivity was observed for Sr-NTO-SS than for NTO-SS, confirming the positive effect of Sr-doping. Figure 4c shows typical fluorescence images captured during the 488 nm laser irradiation of a single Sr-NTO-SS particle on the cover glass in Ar-saturated MS-DN-BODIPY (1 μM) aqueous methanol solution before and after 265-nm light irradiation from the top (Figure 4a). A sudden increase in intensity upon UV irradiation corresponds to the generation of the fluorescent product (i.e., MS-HN-BODIPY) at the bottom surface of the crystal, which was sufficiently excited by an evanescent field (Figure 4a). According to the fact that only the top surface of Sr-NTO-SS was excited by UV light because of a light penetration depth of ~10 nm,[38] it can be suggested that some mobile electrons arrived at the bottom surface of the crystal over the barrier of ~0.1 eV by thermal energy, and eventually reduced the probe molecules within their lifetimes. On the other hand, much weaker

fluorescence signals were observed on the lateral surfaces of NTO-SS particles, again confirming that the photocatalytic performance can be greatly improved by Sr-doping (Figure S8). Interestingly, some Sr-NTO-SS particles exhibited single-molecule-like fluorescence bursts or fluctuation[50] and a gradual increase in fluorescence intensity upon UV irradiation (Figure S9). These results imply a significant difference in the concentration of arriving electrons in individual particles with differing compositions and structures, as evidenced by Figure 3c.

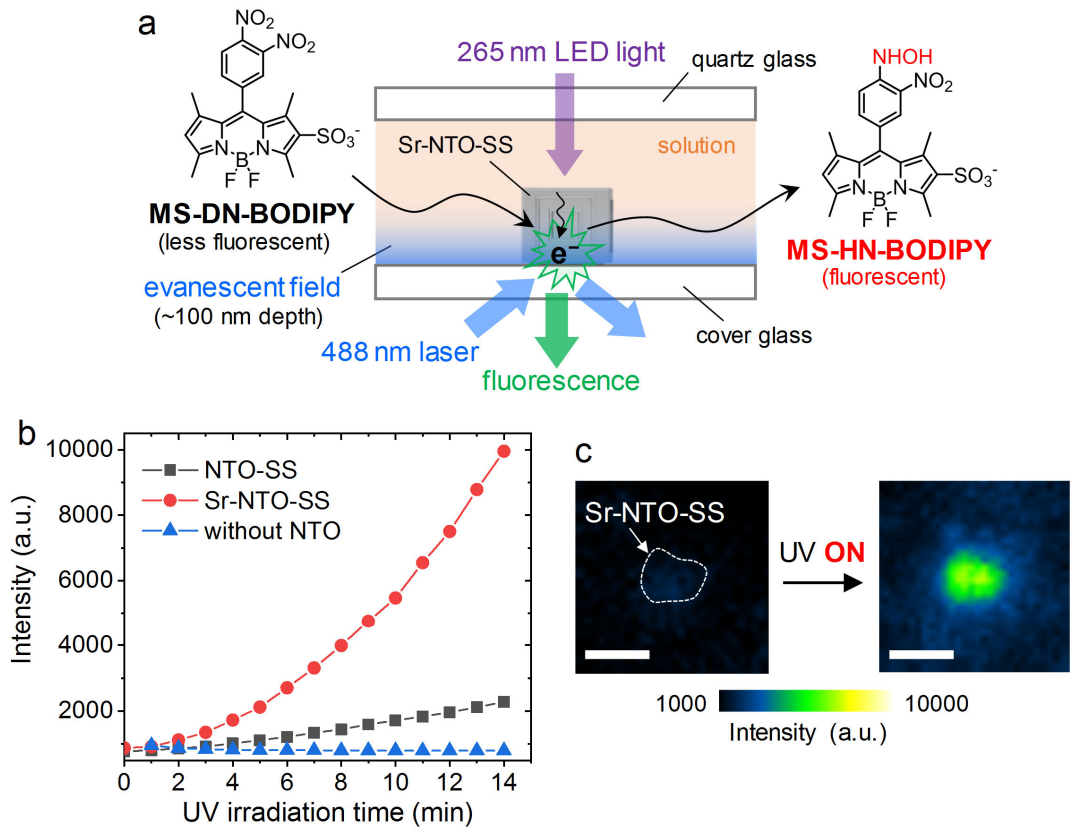

Figure 4. (a) Illustration of photocatalytic generation of fluorescent MS-HN-BODIPY from non-fluorescent MS-DN-BODIPY over a particle. Only the bottom surface of the crystal was excited by evanescent light. (b) UV irradiation time dependence of fluorescence intensity observed at 515 nm for Ar-saturated aqueous methanol solutions of MS-DN-BODIPY (5 μM) in the presence and absence of photocatalysts. (c) Fluorescence images of a single Sr-NTO-SS particle

or aggregate on the cover glass in Ar-saturated aqueous methanol solution of MS-DN-BODIPY (1 μM) under 488 nm laser and 266 nm LED light irradiation. In the left image, the location of the particle is surrounded by a broken line. Scale bars are 1 μm.

Conclusion

We have developed a time-resolved DUV-FM system for the observation of PL from pristine and Sr-doped $NaTaO_3$ crystals at the single-particle level. For Sr-NTO-SS, combined measurements of DUV-FM and TEM-EDS revealed that a certain amount of doped Sr (< 3 mol%) increases the energy level of STEs in $NaTaO_3$ by ~0.1 eV because of the hybridization of Ta 5d and Sr states, and further doping (> 3 mol%) leads to the trapping of excitons or charge carriers at the accompanying deeper states. The Sr-NTO-SS particles exhibited significantly lower PL intensity and shorter lifetime than NTO-SS, suggesting that charge separation was facilitated by the Sr-induced energy gradient near the surface to overcome the trap depth in the exciton. Furthermore, in-situ observation of the photocatalytic reduction reaction over a single Sr-NTO-SS particle revealed that electrons that escaped from the photoexcited surface where the holes are located arrived at the opposite surface to reduce the adsorbed substrates. Our single-particle approach provided strong evidence for the dopant-driven enhancement of charge separation, which will be a promising strategy to improve the efficiency of solar fuel production systems.

Acknowledgment. This work was partially supported by JSPS KAKENHI Grant Numbers JP16H02250, JP18H01944, and others.

References.

1. Chen, X.; Shen, S.; Guo, L.; Mao, S. S. Semiconductor-Based Photocatalytic Hydrogen Generation. *Chem. Rev.* **2010,** *110*, 6503-6570.
2. Nakata, K.; Fujishima, A. TiO_2 Photocatalysis: Design and Applications. *J. Photochem. Photobiol., C* **2012,** *13*, 169-189.
3. White, J. L.; Baruch, M. F.; Pander, J. E., III; Hu, Y.; Fortmeyer, I. C.; Park, J. E.; Zhang, T.; Liao, K.; Gu, J.; Yan, Y.; Shaw, T. W.; Abelev, E.; Bocarsly, A. B. Light-Driven Heterogeneous Reduction of Carbon Dioxide: Photocatalysts and Photoelectrodes. *Chem. Rev.* **2015,** *115*, 12888-12935.
4. Kudo, A.; Miseki, Y. Heterogeneous Photocatalyst Materials for Water Splitting. *Chem. Soc. Rev.* **2009,** *38*, 253-278.
5. Kudo, A.; Kato, H. Effect of Lanthanide-Doping into $NaTaO_3$ Photocatalysts for Efficient Water Splitting. *Chem. Phys. Lett.* **2000,** *331*, 373-377.
6. Kato, H.; Asakura, K.; Kudo, A. Highly Efficient Water Splitting into H_2 and O_2 over Lanthanum-Doped $NaTaO_3$ Photocatalysts with High Crystallinity and Surface Nanostructure. *J. Am. Chem. Soc.* **2003,** *125*, 3082-3089.
7. Iwase, A.; Kato, H.; Okutomi, H.; Kudo, A. Formation of Surface Nano-Step Structures and Improvement of Photocatalytic Activities of $NaTaO_3$ by Doping of Alkaline Earth Metal Ions. *Chem. Lett.* **2004,** *33*, 1260-1261.
8. Iwase, A.; Kato, H.; Kudo, A. The Effect of Alkaline Earth Metal Ion Dopants on Photocatalytic Water Splitting by $NaTaO_3$ Powder. *ChemSusChem* **2009,** *2*, 873-877.
9. Chiang, T. H.; Lyu, H.; Hisatomi, T.; Goto, Y.; Takata, T.; Katayama, M.; Minegishi, T.; Domen, K. Efficient Photocatalytic Water Splitting Using Al-Doped SrTiO3 Coloaded with Molybdenum Oxide and Rhodium-Chromium Oxide. *ACS Catal.* **2018,** *8*, 2782-2788.
10. Onishi, H. Sodium Tantalate Photocatalysts Doped with Metal Cations: Why are They Active for Water Splitting? *ChemSusChem* **2019**, Ahead of Print.
11. Kato, H.; Kudo, A. Water Splitting into H_2 and O_2 on Alkali Tantalate Photocatalysts $ATaO_3$ (A = Li, Na, and K). *J. Phys. Chem. B* **2001,** *105*, 4285-4292.
12. Zhang, G.; Liu, G.; Wang, L.; Irvine, J. T. S. Inorganic Perovskite Photocatalysts for Solar Energy Utilization. *Chem. Soc. Rev.* **2016,** *45*, 5951-5984.
13. Linsebigler, A. L.; Lu, G.; Yates, J. T., Jr. Photocatalysis on TiO_2 Surfaces: Principles, Mechanisms, and Selected Results. *Chem. Rev.* **1995,** *95*, 735-58.
14. Schneider, J.; Matsuoka, M.; Takeuchi, M.; Zhang, J.; Horiuchi, Y.; Anpo, M.; Bahnemann, D. W. Understanding TiO_2 Photocatalysis: Mechanisms and Materials. *Chem. Rev.* **2014,** *114*, 9919-9986.
15. An, L.; Onishi, H. Electron-Hole Recombination Controlled by Metal Doping Sites in $NaTaO_3$ Photocatalysts. *ACS Catal.* **2015,** *5*, 3196-3206.
16. An, L.; Park, Y.; Sohn, Y.; Onishi, H. Effect of Etching on Electron-Hole Recombination in Sr-Doped $NaTaO_3$ Photocatalysts. *J. Phys. Chem. C* **2015,** *119*, 28440-28447.
17. An, L.; Sasaki, T.; Weidler, P. G.; Woll, C.; Ichikuni, N.; Onishi, H. Local Environment of Strontium Cations Activating $NaTaO_3$ Photocatalysts. *ACS Catal.* **2018,** *8*, 880-885.
18. Empedocles, S. A.; Neuhauser, R.; Shimizu, K.; Bawendi, M. G. Photoluminescence from Single Semiconductor Nanostructures. *Adv. Mater.* **1999,** *11*, 1243-1256.

19. Jing, L.; Qu, Y.; Wang, B.; Li, S.; Jiang, B.; Yang, L.; Wei, F.; Fu, H.; Sun, J. Review of Photoluminescence Performance of Nano-Sized Semiconductor Materials and Its Relationships with Photocatalytic Activity. *Sol. Energy Mater. Sol. Cells* **2006,** *90*, 1773-1787.
20. Klimov, V. I. Spectral and Dynamical Properties of Multiexcitons in Semiconductor Nanocrystals. *Annu. Rev. Phys. Chem.* **2007,** *58*, 635-673.
21. Matsuoka, M.; Saito, M.; Anpo, M. Photoluminescence spectroscopy. *Charact. Solid Mater. Heterog. Catal.* **2012,** *1*, 149-184.
22. Zhang, Z.; Yates, J. T., Jr. Band Bending in Semiconductors: Chemical and Physical Consequences at Surfaces and Interfaces. *Chem. Rev.* **2012,** *112*, 5520-5551.
23. Tachikawa, T.; Majima, T. Single-Molecule, Single-Particle Fluorescence Imaging of TiO_2-Based Photocatalytic Reactions. *Chem. Soc. Rev.* **2010,** *39*, 4802-4819.
24. Chen, P.; Zhou, X.; Shen, H.; Andoy, N. M.; Choudhary, E.; Han, K.-S.; Liu, G.; Meng, W. Single-Molecule Fluorescence Imaging of Nanocatalytic Processes. *Chem. Soc. Rev.* **2010,** *39*, 4560-4570.
25. De Cremer, G.; Sels, B. F.; De Vos, D. E.; Hofkens, J.; Roeffaers, M. B. J. Fluorescence Micro(spectro)scopy as a Tool to Study Catalytic Materials in Action. *Chem. Soc. Rev.* **2010,** *39*, 4703-4717.
26. Yamakata, A.; Ishibashi, T.; Kato, H.; Kudo, A.; Onishi, H. Photodynamics of $NaTaO_3$ Catalysts for Efficient Water Splitting. *J. Phys. Chem. B* **2003,** *107*, 14383-14387.
27. Wiegel, M.; Emond, M. H. J.; Stobbe, E. R.; Blasse, G. Luminescence of Alkali Tantalates and Niobates. *J. Phys. Chem. Solids* **1994,** *55*, 773-8.
28. Lee, Y.-C.; Teng, H.; Hu, C.-C.; Hu, S.-Y. Temperature-Dependent Photoluminescence in $NaTaO_3$ with Different Crystalline Structures. *Electrochem. Solid-State Lett.* **2008,** *11*, P1-P4.
29. Hu, C.-C.; Tsai, C.-C.; Teng, H. Structure Characterization and Tuning of Perovskite-Like $NaTaO_3$ for Applications in Photoluminescence and Photocatalysis. *J. Am. Ceram. Soc.* **2009,** *92*, 460-466.
30. Williams, R. T.; Song, K. S. The Self-Trapped Exciton. *J. Phys. Chem. Solids* **1990,** *51*, 679-716.
31. Grushka, E. Characterization of Exponentially Modified Gaussian Peaks in Chromatography. *Anal. Chem.* **1972,** *44*, 1733-1738.
32. Pezzoli, F.; Qing, L.; Giorgioni, A.; Isella, G.; Grilli, E.; Guzzi, M.; Dery, H. Spin and Energy Relaxation in Germanium Studied by Spin-Polarized Direct-Gap Photoluminescence. *Phys. Rev. B* **2013,** *88*, 045204/1-045204/12.
33. McCall, K. M.; Stoumpos, C. C.; Kostina, S. S.; Kanatzidis, M. G.; Wessels, B. W. Strong Electron-Phonon Coupling and Self-Trapped Excitons in the Defect Halide Perovskites $A_3M_2I_9$ (A = Cs, Rb; M = Bi, Sb). *Chem. Mater.* **2017,** *29*, 4129-4145.
34. Watanabe, M.; Hayashi, T. Time-Resolved Study of Self-Trapped Exciton Luminescence in Anatase TiO_2 under Two-Photon Excitation. *J. Lumin.* **2005,** *112*, 88-91.
35. Leonelli, R.; Brebner, J. L. Time-Resolved Spectroscopy of the Visible Emission Band in Strontium Titanate. *Phys. Rev. B* **1986,** *33*, 8649-8656.
36. Katayama, I.; Tanaka, K. Nature and Dynamics of Photoexcited States in $KTaO_3$. *J. Phys. Soc. Jpn.* **2006,** *75*, 064713/1-064713/12.
37. An, L.; Onishi, H. Rate of Ag Photodeposition on Sr-Doped $NaTaO_3$ Photocatalysts as Controlled by Doping Sites. *e-J. Surf. Sci. Nanotechnol.* **2015,** *13*, 253-255.

38. An, L.; Kitta, M.; Iwase, A.; Kudo, A.; Ichikuni, N.; Onishi, H. Photoexcited Electrons Driven by Doping Concentration Gradient: Flux-Prepared $NaTaO_3$ Photocatalysts Doped with Strontium Cations. *ACS Catal.* **2018,** *8*, 9334-9341.
39. Wiegel, M.; Hamoumi, M.; Blasse, G. Luminescence and Nonlinear Optical Properties of Perovskite-Like Niobates and Titanates. *Mater. Chem. Phys.* **1994,** *36*, 289-293.
40. Hu, C.-C.; Lee, Y.-L.; Teng, H. Efficient Water Splitting over $Na_{1-x}K_xTaO_3$ Photocatalysts with Cubic Perovskite Structure. *J. Mater. Chem.* **2011,** *21*, 3824-3830.
41. Liu, X.; Sohlberg, K. Role of Effective Carrier Mass in the Photocatalytic Efficiency of La-Doped $NaTaO_3$. *Comput. Mater. Sci.* **2016,** *123*, 1-7.
42. Lin, W.-H.; Cheng, C.; Hu, C.-C.; Teng, H. $NaTaO_3$ Photocatalysts of Different Crystalline Structures for Water Splitting into H_2 and O_2. *Appl. Phys. Lett.* **2006,** *89*, 211904/1-211904/3.
43. Hu, C.-C.; Teng, H. Influence of Structural Features on the Photocatalytic Activity of $NaTaO_3$ Powders from Different Synthesis Methods. *Appl. Catal., A* **2007,** *331*, 44-50.
44. Choi, M.; Oba, F.; Tanaka, I. First-Principles Study of Native Defects and Lanthanum Impurities in $NaTaO_3$. *Phys. Rev. B* **2008,** *78*, 014115/1-014115/8.
45. Wang, H.; Wu, F.; Jiang, H. Electronic Band Structures of $ATaO_3$ (A = Li, Na, and K) from First-Principles Many-Body Perturbation Theory. *J. Phys. Chem. C* **2011,** *115*, 16180-16186.
46. Sayama, K.; Mukasa, K.; Abe, R.; Abe, Y.; Arakawa, H. A New Photocatalytic Water Splitting System under Visible Light Irradiation Mimicking a Z-Scheme Mechanism in Photosynthesis. *J. Photochem. Photobiol. C* **2002,** *148*, 71-77.
47. Tamaki, Y.; Furube, A.; Murai, M.; Hara, K.; Katoh, R.; Tachiya, M. Direct Observation of Reactive Trapped Holes in TiO_2 Undergoing Photocatalytic Oxidation of Adsorbed Alcohols: Evaluation of the Reaction Rates and Yields. *J. Am. Chem. Soc.* **2006,** *128*, 416-417.
48. Knorr, F. J.; Mercado, C. C.; McHale, J. L. Trap-State Distributions and Carrier Transport in Pure and Mixed-Phase TiO_2: Influence of Contacting Solvent and Interphasial Electron Transfer. *J. Phys. Chem. C* **2008,** *112*, 12786-12794.
49. Longo, E.; Orhan, E.; Pontes, F. M.; Pinheiro, C. D.; Leite, E. R.; Varela, J. A.; Pizani, P. S.; Boschi, T. M.; Lanciotti, F., Jr.; Beltran, A.; Andres, J. Density Functional Theory Calculation of the Electronic Structure of $Ba_{0.5}Sr_{0.5}TiO_3$: Photoluminescent Properties and Structural Disorder. *Phys. Rev. B Condens. Matter Mater. Phys.* **2004,** *69*, 125115/1-125115/7.
50. Tachikawa, T.; Yonezawa, T.; Majima, T. Super-Resolution Mapping of Reactive Sites on Titania-Based Nanoparticles with Water-Soluble Fluorogenic Probes. *ACS Nano* **2013,** *7*, 263-275.